Computational Methods and Theoretical Results for the Ka-Band Array Feed Compensation System–Deformable Flat Plate Experiment at DSS 14

W. A. Imbriale[1] and D. J. Hoppe[1]

This article documents the computational methods and theoretical results for the deformable flat plate (DFP), array feed compensation system (AFCS), monopulse tracking system, and combined AFCS–DFP used for compensating the gravity-induced distortions on the DSN's 70-m antenna. These systems were utilized in an experiment designed to verify gravity compensation and tracking performance of the 70-m antenna at 31.8–32.2 GHz (Ka-band). This experiment took place from November 1998 through February 1999 and consisted of both quasar and spacecraft observations. The theoretical results are compared with the experimental data. The analytical tools are also used to document and understand the characteristics of each system.

I. Introduction

During the period from November 1998 through February 1999, a series of measurements was carried out on the 70-m antenna at DSS 14 to determine the performance characteristics of two systems designed to compensate for the effects of elevation-dependent gravity distortion of the main reflector on antenna gain. The array feed compensation system (AFCS) and the deformable flat plate (DFP) system both were mounted on the same feed cone, and each was used independently as well as jointly to measure and improve the antenna aperture efficiency as a function of elevation angle. The experimental data are presented in [1] and [2].

This article contains a description of the computational method and theoretical results for the DFP, the AFCS, the monopulse tracking system, and the combined AFCS–DFP system.

The basic analysis tool is a physical optics reflector-analysis code that was ported to a parallel computer for faster execution times. There are several steps involved in computing the RF performance of the various systems:

---

[1] Communications Ground Systems Section.

(1) A model of the RF distortions of the main reflector is required. This model is based upon measured holography maps of the 70-m antenna obtained at three elevation angles. The holography maps then are processed (using an appropriate gravity mechanical model of the dish) to provide surface distortion maps at all elevation angles. This technique is further described in [3].

(2) From the surface distortion maps, ray optics is used to determine the theoretical shape of the DFP that will exactly phase compensate the distortions.

(3) From the theoretical shape and a NASTRAN mechanical model of the plate, the actuator positions that generate a surface that provides the best rms fit to the theoretical model are selected. Using the actuator positions and the NASTRAN model provides an accurate description of the actual mirror shape.

(4) Starting from the mechanical drawings of the feed, a computed RF feed pattern is generated. This pattern is expanded into a set of spherical wave modes so that a complete near-field analysis of the reflector system can be obtained.

(5) For the array feed, the excitation coefficients that provide the maximum gain are computed using a phase conjugate technique.

The basic experimental geometry consisted of a dual-shaped 70-m antenna system, a refocusing ellipse, a DFP, and an array feed system. To provide physical insight into the systems performance, focal plane field plots are presented at several elevations. Curves of predicted performance are shown for the DFP system, monopulse tracking system, AFCS, and combined DFP–AFCS system. The calculated results show that the combined DFP–AFCS system is capable of recovering the majority of the gain lost due to gravity distortion.

II. Geometry

The experiment geometry is shown in Fig. 1. The main elements are the 70-m main reflector and subreflector, a refocusing ellipse, the DFP, and the receive feed system. The focal point of the dual-reflector 70-m system is labeled F_1, and the focal point where the feed is placed is labeled F_2. The antenna Cassegrain focus was 0.6 in. (1.5 cm) above F_1, which was corrected for alignment of the subreflector in the z-axis. Looking at the system in the transmit mode, the output of the feed system is refocused at F_1, the input to the dual-reflector system. The parameters of the ellipse are chosen to map the fields (with no magnification) from F_2 to F_1. Hence, the performance of the 70-m system would be the same if the same feed were placed at either F_1 or F_2.

A. Ray-Based Computation of the Deformable-Mirror Surface

In this section, a description of the steps involved in the computation of the deformable-mirror surface is provided. The process begins with a processed holography map describing the main-reflector distortions to be corrected for at the elevation angle of interest. The final output of the design process is the surface of the deformable mirror required to correct for those distortions. Three main computer programs are involved. The process is summarized in the flow chart presented in Fig. 2 and in the following paragraphs.

1. Step 1: Zernike Coefficient Computation. The first step in the design process is to process the holography maps described earlier in the article for use in the computation. Due to the large size of the reflectors relative to the wavelength at 32 GHz, it was decided to ignore diffraction in the computation of the deformable-mirror surface. A ray-based analysis code, Modeling and Analysis for Controlled Optical Systems (MACOS) [4], is used to trace the deformations on the main reflector to the deformable mirror. With MACOS, arbitrary surfaces such as the distorted-shaped reflectors of DSS 14 are described using a Zernike expansion. The nominal shaped subreflector and main-reflector surfaces and the main-reflector distortion require Zernike expansions.
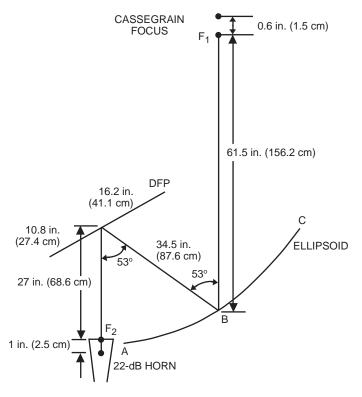
Fig. 1. The RF optics design inside the holography cone, showing the geometry that enables both separate AFCS and DFP measurements at F_1 and F_2, respectively, and joint AFCS–DFP measurements at F_2.

As illustrated in Fig. 2, the program DFM.EXE computes the Zernike coefficients for a given main-reflector distortion. The distortion is described via a processed holography map, typically on a 127-by-127 point square grid encompassing the main reflector. Additional information such as the grid spacing, frequency, reflector diameter, and best-fit parabola are included in an additional data file. This data file also includes details regarding any masks that must be applied to the holography map. Shadowed areas of the main reflector are masked. These included strut shadows and the center of the reflector where the tricone structure is located. These areas receive essentially zero amplitude illumination and, hence, the phase data in these areas cannot be used to deduce the surface distortion. The masks are employed as follows. The main-reflector distortions in the masked areas are initially set to zero. An initial Zernike series is computed. The Zernike series then is used to fill in an approximate distortion in the masked areas, and a new Zernike series is computed. The process is repeated until convergence of the Zernike coefficients is achieved. Less than 10 iterations of this process results in a smooth extrapolation of the surface distortion into the masked areas.

The deformable-mirror surfaces computed for this work were based on including 91 terms in the Zernike expansion of the main-reflector distortions. Although including more terms would better model higher-order surface distortions in the main reflector, including them was found to have essentially no impact on the final actuator positions computed for the deformable mirror. This is expected since the actuator density on the mirror determines the scale of distortion that may be corrected. In this case, the resolution of the actuators is already greatly exceeded by the 91-term Zernike expansion of the main-reflector distortion.
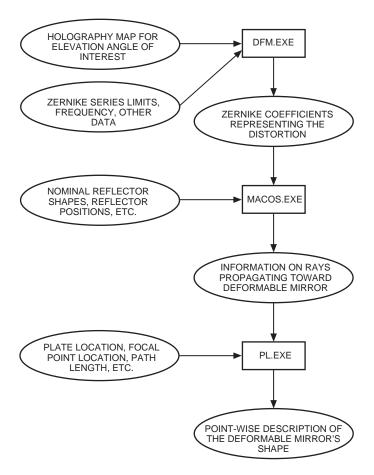
Fig. 2. Flow chart describing the computation of the deformable mirror.

2. Step 2: Ray Trace of the Distorted-Reflector System. As mentioned above, due to the large size of the reflectors on DSS 14 in terms of wavelengths at 32 GHz, a ray-based approach to determining the deformable-mirror surface is deemed satisfactory. The validity of this assumption is tested in a subsequent section of this article, where physical optics (PO), which takes into account diffraction effects, is used to evaluate the performance of the system. A modified version of MACOS, a JPL-produced code, was used to trace the rays through the distorted-reflector system. The code was modified to increase the maximum number of terms in the Zernike expansion of the surfaces. Due to details regarding the manner in which arbitrary surfaces are handled in MACOS, this modification turned out to be non-trivial.

As illustrated in Fig. 2, the Zernike coefficients for the distortion are combined with the file describing the nominal-reflector system geometry and fed into MACOS. The shaped subreflector and main reflector are described by 21-term, rotationally symmetric, Zernike expansions. The additional Zernike terms describing the deformation then are added to the nominal main-reflector surface description. The ellipsoid, which refocuses the incoming radiation through the deformable mirror to the remote feed location, also is included in the model. All hardware locations and rotations are included in the model.

The analysis begins by launching a bundle of approximately 4000 rays into the main reflector. Masks are applied, limiting the maximum diameter of the main reflector and subreflector. An additional mask is applied to eliminate the tricone area of the main-reflector surface. The rays are traced to the subreflector and finally to the ellipsoid, where they are reflected toward the deformable mirror. Figure 3 shows a low-resolution two-dimensional plot of the reflector geometry and a subset of rays. The output capabilities of
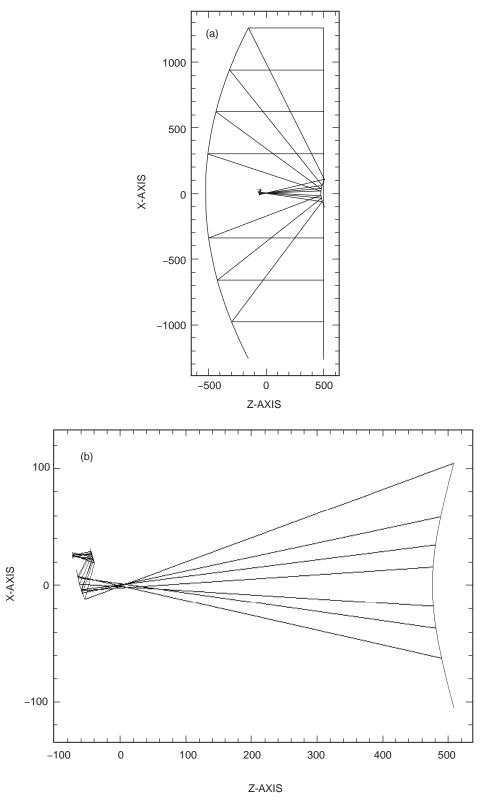
Fig. 3. Ray traces: (a) main reflector to focal plane and (b) subreflector to focal plane.

MACOS then are employed to generate an output file containing the ray positions, directions, and ray-path lengths immediately after reflection from the ellipsoid. For a typical run, this file contains information on approximately 3200 rays that survive the masking operations. The ray information contained in this file then is employed in the last step of the process, as described below.

3. Step 3: Computation of the Deformable-Mirror Surface. The final step in the calculation is performed in the program PL.EXE, as illustrated in Fig. 2. The ray information from MACOS is combined with information on the location of the center of the deformable mirror, the required focal point for the ray bundle, and the overall path length required. For each ray, a point on the deformable-mirror surface is determined as described below. A file consisting of a point-wise description of the deformable mirror containing approximately 3200 data points finally is produced. Figure 4 shows an example deformable-mirror distortion profile, interpolated and plotted with Matlab.

Points on the deformable mirror are computed using a simple algorithm. Starting at the ellipsoid, each ray is propagated forward toward the deformable mirror until the distance propagated plus the distance to the required focal point is equal to the overall path length required. For an undistorted main reflector, this process results in a tilted flat plate. This simple path-length-based algorithm was used to compute the deformable-mirror surface for each elevation angle of interest. The validity of this simple algorithm will be assessed in a later portion of this article via a physical optics analysis of the entire antenna system with the deformed mirror in place. As is discussed later in this article, the "ideal" deformable-mirror surface so determined is used along with the x- and y-coordinate locations of the actuators to arrive at the best set of z-axis displacements. The various approximations and limitations of the ray-trace approach are discussed below.
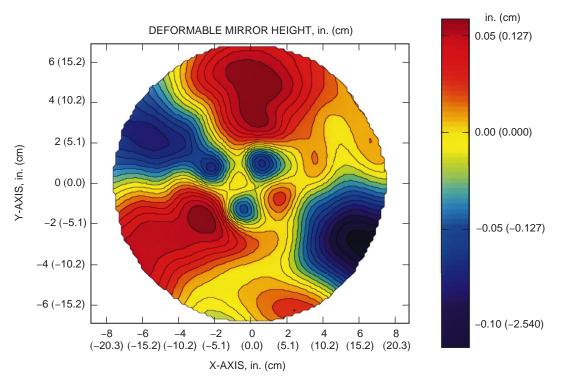

Fig. 4. A sample computed deformable-mirror surface.

4. Discussion of Limitations. A number of limitations in the above design procedure need to be discussed. One basic limitation is in the decision to ignore diffraction entirely and to use a ray-based approach. As was discussed above, the penalty paid for ignoring diffraction is not significant and will be computed exactly in a later section. Another limitation is that only a finite number of rays are used to define the mirror surface. This limitation is not significant since the surface described by 3200 rays contains details not resolvable by the finite number of actuators in the actual deformable mirror.

The most significant limitations involve the description of the reflector surfaces in terms of a finite Zernike series. The main-reflector distortions are described to a level exceeding that required for determining the actuator positions. Since the surfaces are shaped rather than being a conventional hyperbola/parabola, the undistorted main-reflector and subreflector surfaces also are described by a finite Zernike series. A ray trace of the undistorted system reveals that a perfect focus is not achieved using only 21 circularly symmetric terms in the representation of the shaped reflectors. The major source of error is in the representation of the subreflector near its apex. In this region, the slope of the subreflector is discontinuous due to the presence of the vertex plate. The vertex plate directs rays away from the tricone area in the center of the main reflector. Such a surface is not well described in this region by a finite-length Zernike series. The impact of this limitation in the description of the subreflector is also small, as reflected in the physical optics calculations. In the future, it would be beneficial to investigate methods for inserting a better model for the undistorted reflectors into MACOS.

B. Perfect, Actual, and Measured Plates

The output of the ray-tracing analysis provides the so-called perfect-plate geometry, the geometry that will, in a ray-trace sense, perfectly phase compensate for the distortion. The actual DFP is made up of a thin aluminum sheet backed by 16 actuators (see Fig. 5) whose locations were originally chosen to compensate for the distortion of the DSN 34-m antenna and do not optimally match the desired shapes that compensate the 70-m antenna. A computer program does exist (derived from the analysis described in [5]), however, to predict the actuator displacement values that produce a plate surface that best fits the desired perfect-plate geometry. Using the best-fit actuator displacements, the surface shape of the actual DFP can be determined. This is the predicted shape of the actual mirror and is the best that can be done with the existing 16 actuators. An example of the process is shown in Fig. 6. Figure 6(a) is the perfect plate geometry and is defined only over the portion of the plate that intercepts the rays reflected from the main reflector. The rays intercept a diameter of only about 18 in. (46 cm), whereas the actual plate is 27 in. (68.6 cm) in diameter. Figure 6(b) is the predicted shape based upon actuator displacements that best fit the desired shape. Figure 6(c) is a measurement of the actual plate geometry and is within 0.010 in. (0.25 mm) rms of the calculated shape.

III. Physical Optics Computational Techniques

The basic analysis technique used is the physical optics program described in [6]. For computational speed, the program was converted to run in parallel on the California Institute of Technology exemplar computer where, on 128 processors, it runs over 100 times faster than on a 266-MHz Pentium Pro computer.

The undistorted asymmetric 70-m dual-reflector system is approximated by a symmetric system since a drawing of the subreflector with sufficient accuracy for 32 GHz (Ka-band) was not available. However, based on analysis of similar systems, the error introduced by using a symmetric system instead of the actual asymmetric system should be very small and would not alter the basic conclusions. The main-reflector distortions are modeled by a set of Zernike polynomials derived from the processed holography maps [3]. The feed patterns are computed using the corrugated feed program and an exact mechanical description of the feed.
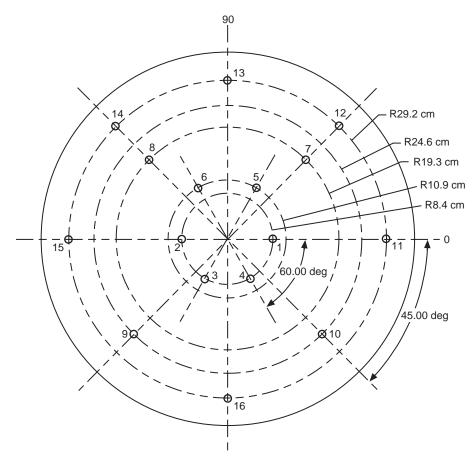
Fig. 5. DFP actuator locations (looking at the mirror face).

The 16-actuator plate geometry is derived from the ray-based theoretical description (previous section) and a computer program [5] that computes the actual shape based upon actuator locations and a finite-element model of the mechanical plate. The perfect plate uses a smoothed version of the theoretical description.

For various reasons, there were additional approximations used in computing the performance of the DFP. Since, when the initial calculations were performed, the errors in the geometry regarding the position of the ellipse were not known, the errors in the tilt and location of the ellipse relative to the intended geometry are not included. Also, the DFP surfaces used in the experiment were generated assuming the DFP was positioned 30 in. (76.2 cm) from the F_2 ellipse focal point, not the actual geometry of 28 in. (71.1 cm). Although these differences will lead to some reductions in the DFP performance, it is expected that the error will be small and will not alter the conclusions of the experiment.

IV. Focal Plane Analysis

To provide some insight into the performance of the various systems, the focal fields are displayed for several conditions. Figure 7 shows the focal plane fields for an undistorted system. It is easy to envision that a single feed horn with the proper spot size would be optimal for this system. It should be noted that none of the auxiliary rings associated with an Airy pattern are present. They are not present in the dual-shaped reflector system. Figures 8 through 10 show the focal plane fields are significantly spread out for the distorted cases over the focal plane region, especially for the 85-deg case. Also shown on the 85-deg-elevation map is an outline of the 7-element array feed. For this case, it is obvious that
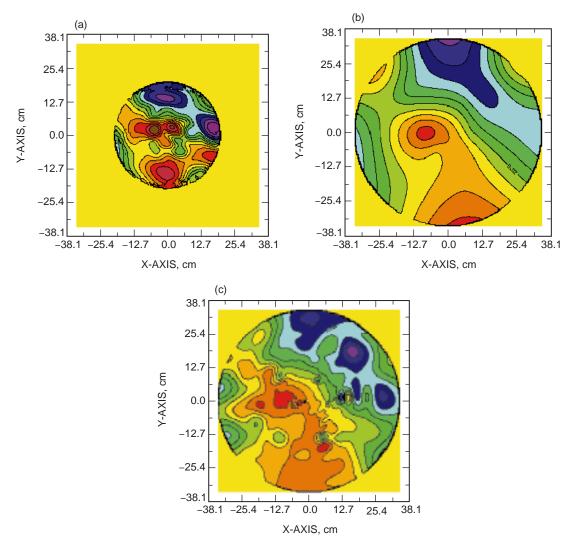
Fig. 6. Plate geometry for 12.7-deg elevation: (a) perfect, (b) actual, and (c) measured.

there is significant spillover past the feed horns, limiting the possible improvement of the current array feed. Figures 11 through 13 show the results at F_2 for the case of the 16-actuator plate and the smoothed theoretical plate. Observe that the focal plane spread has been significantly reduced. Also observe that the theoretical plate provides nearly complete compensation.

V. Baseline Efficiency

The baseline efficiency was measured at both the F_1 and F_2 focal points. At F_1, the center feed of the AFCS was used, and, at F_2, the standard 22.5-dBi horn was used. See [1] for a complete description of the data analysis. Using the expected gain difference between F_1 and F_2, the data at F_2 were referenced to F_1 and plotted on the same graph (see Fig. 14). Using the all-elevation-angle holography model of the antenna distortion, a complete physical optics analysis was made, predicting antenna performance versus elevation angle. The computed efficiency is the combination of factors not directly included in the physical optics program plus the computation of the efficiency due to the modeled geometry and main-reflector surface shape. The items not directly included in the PO computation are summarized in Table 1. The most significant term is the projection of the medium-resolution holography rms results
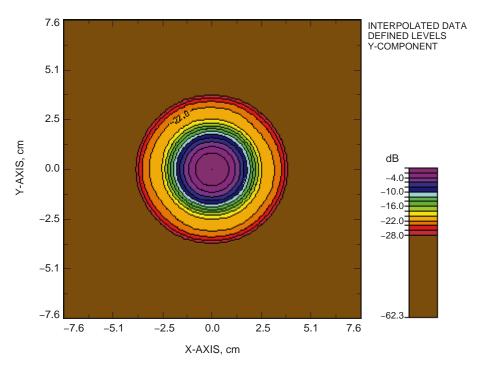
Fig. 7. Focal plane distribution of the undistorted dual-reflector system.
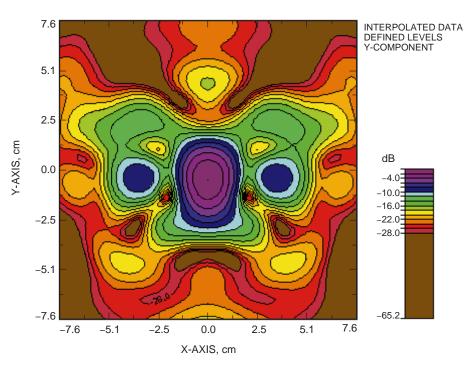

Fig. 8. Focal plane distribution of the dual-reflector system, elevation = 15 deg.
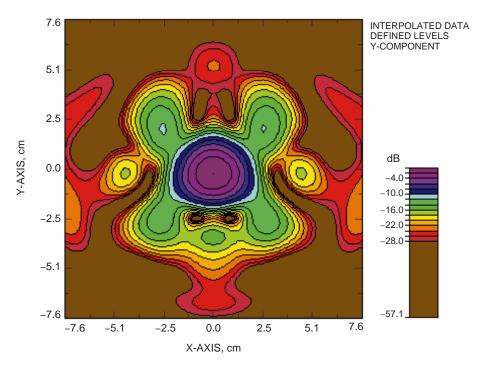
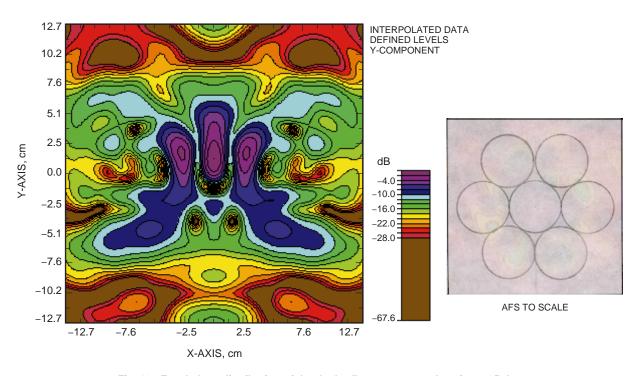**Fig. 9. Focal plane distribution of the dual-reflector system, elevation = 45 deg.**

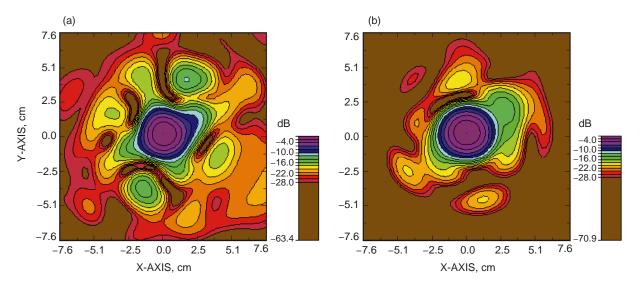**Fig. 10. Focal plane distribution of the dual-reflector system, elevation = 85 deg.**

11

Fig. 11. Focal plane distribution at F_2, elevation = 15 deg (interpolated data, defined levels, y-component): (a) actual plate and (b) smoothed perfect plate.
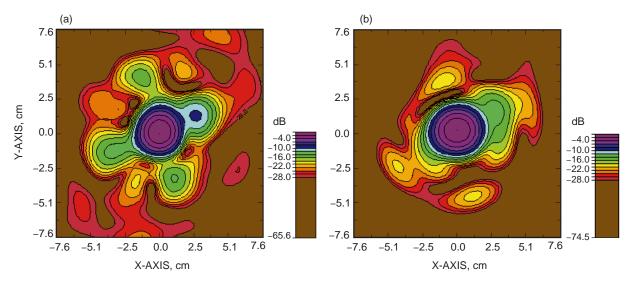
Fig. 12. Focal plane distribution at F_2, elevation = 45 deg (interpolated data, defined levels, y-component): (a) actual plate and (b) smoothed perfect plate.

to infinite-resolution rms. This is due to the fact that the medium-resolution maps do not contain all the very high-order random rms distortions, and this additional loss must be accounted for separately. The number is based upon comparison of the rms from measured low, medium and high resolution at the rigging angle and projecting the curve to infinite-resolution rms. The three-angle holography data are only medium resolution; hence, it is necessary to include the loss due to the missing very high-order random distortions.

Figure 14 contains two computed differences—the efficiency due to using the Zernike polynomial description of the main reflector and the efficiency using the full medium-resolution holography maps. As can be seen, there is a significant amount of loss not accounted for by the Zernike polynomial description of the main-reflector surface.
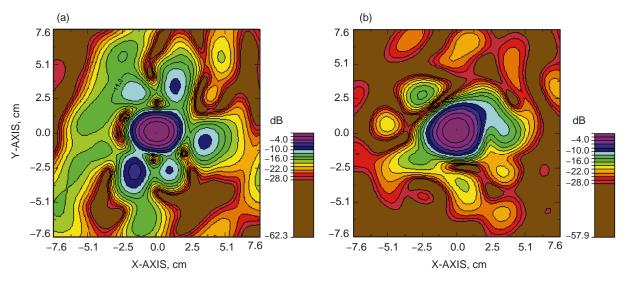
12

Fig. 13. Focal plane distribution at F_2, elevation = 85 deg (interpolated data, defined levels, y-component): (a) actual plate and (b) smoothed perfect plate.
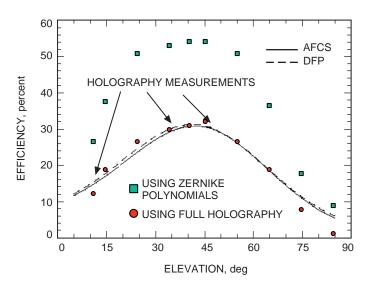

Fig. 14. Predicted and measured baseline performance of the 70-m antenna at Ka-band.

VI. Comparison of Computed Versus Measured Results

The computed versus measured results for the array feed at F_1 are shown in Fig. 15. The data represent the gain improvement obtained by using the seven-element array feed over the power in the center element alone. Two cases are shown—one using the Zernike polynomial representation of the main dish and the other using the full holography maps. Even though there is a significant gain difference between the Zernike polynomials and the full holography maps (see Fig. 12), there is only a very modest improvement in the array feed performance. This indicates that the higher-order distortions in the full holography maps versus the Zernike polynomial description cannot be compensated by the array feed.

Table 1. DSS 14 estimated efficiency performance at Ka-band without compensation (rigging angle approximately 42 deg).

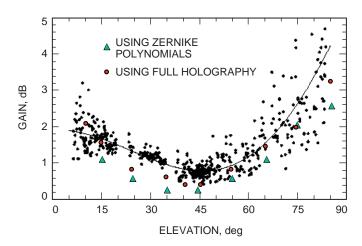| Item	Ka-band
Main reflector dissipative loss	0.9991
Panel leak	0.9975
Panel gap	0.9982
Subreflector dissipative loss	0.9991
Beam squint	0.9954
Subreflector focus	1.0000
Cassegrain VSWR (voltage standing-wave ratio) loss	0.9990
Medium-resolution holography rms to infinite	0.7776
Terms not in PO computation	0.767

Fig. 15. **Predicted and measured AFCS compensation.**

The computed versus measured results for the DFP compensation are shown in Fig. 16. Both the computed and measured results represent the difference between the DFP in the flat (uncompensated) and flexed (compensated) modes. Since the derivation of the shape of the DFP used only the Zernike polynomial representation of the main-dish distortion, only small differences were expected between calculated results with either surface representation.

The computed versus measured results for the combined DFP–AFCS are shown in Fig. 17. There are several curves shown on the figure. The lower solid curve is the measured baseline efficiency. The calculated results for the combined DFP–AFCS using the full holography maps are shown in circles, and the calculated results using the Zernike polynomial representation of the surface are shown as triangles. The gain using the Zernike polynomial surface description has been reduced by 3.4 dB to account for the loss due to the random component of the surface not included in the Zernike polynomial representation of the surface. The measured performance of the combined DFP–AFCS system is shown, but only data for lower elevation angles were obtained. Observe that the measured and calculated values agree to within a few percent. Also observe that the combined system recovers almost all of the gain lost due to the systematic distortion (represented by the Zernike polynomial description of the surface) but does
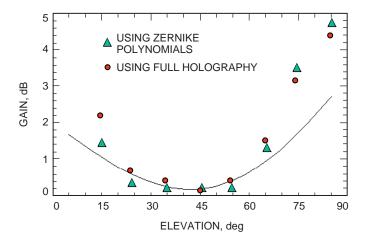
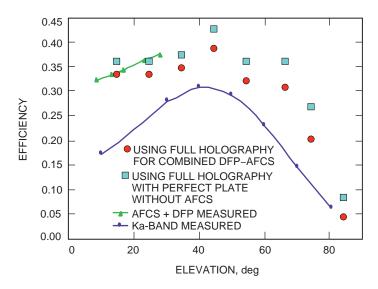**Fig. 16. Predicted and measured DFP compensation (actual plate).**

Fig. 17. Predicted and measured compensation with the combined DFP–AFCS (70-m antenna efficiency at Ka-band).

not recover the random component of the surface distortion (the 3.4-dB difference between the Zernike polynomial and the full holography maps). It is anticipated that a majority of the random component will be recovered by resetting the main reflector.

Also shown in Fig. 17 is the expected performance if a so-called "perfect DFP" were used. A perfect DFP means that the required shape of the plate as determined by the Zernike polynomial expansion of the main-reflector surface is replicated exactly. With an improved DFP, it should be possible to get close to the required surface and produce performance close to this prediction. Observe that the perfect DFP does not recover the random component of the distortion, as this distortion is not even included in its determination.

VII. System Characteristics

Each (DFP or AFCS) system has different characteristics, and the intent of this section is to use the analytical tools to further understand and document these differences. The section will consist of a statement of the characteristic and an explanation or proof of the validity of the statement.

(1) The current analytical model used for the main-reflector shape does not contain all the distortion.

The Zernike polynomial description of the main-reflector surface shape was used to design the DFP. It is obvious from Fig. 14 that this description of the main-reflector surface shape is several dB short of the actual loss in the 70-m antenna. Even the full medium holography description falls 1.15-dB short of the actual losses (see Table 1). A picture of the 15-deg elevation-angle surface is shown in Fig. 18. Figure 18(a) shows the Zernike polynomial
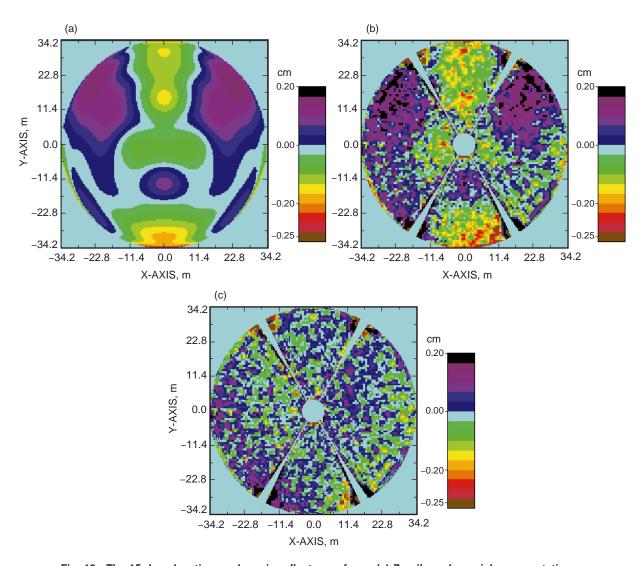

Fig. 18. The 15-deg elevation-angle main-reflector surface: (a) Zernike polynomial representation (raw data, autolevel on, y-component) (b) full holography (raw data, user-specified levels, y-component), and (c) the difference between the two surfaces (raw data, user-specified levels, y-component).

characterization, Fig. 18(b) the full holography representation, and Fig. 18(c) the difference between the two surfaces. Observe that this difference is a very random surface and that neither the AFCS nor the DFP accurately compensates for this random component of the distortion. This random component can be greatly reduced by resetting the main-reflector surface.

(2) The DFP requires an accurate description of the main-reflector surface shape; the AFCS does not.

As seen in the earlier description of the design of the DFP, the basic determination of the DFP requires knowledge of the surface. The AFCS uses the measured signals from the feeds to determine the correct combining weights and does not need to know the shape of the surface to maximize the received signal. However, knowledge of the surface is required for performance prediction.

(3) For the larger distortions, energy spills past the AFCS, but not past the DFP.

It is clear from the focal plane plots (see especially Fig. 10 for 85-deg distortion) that, for the larger distortion cases, there is significant energy in the focal plane outside the range of the AFCS. This also can be seen in plots where a bundle of rays are traced from the reflector to the focal plane, as in Fig. 19. For the DFP (Fig. 20), all rays and, consequently, all the energy are captured by the DFP. This is because the location selected for the DFP is in a position where there is a mapping of the dual-reflector system onto the DFP.
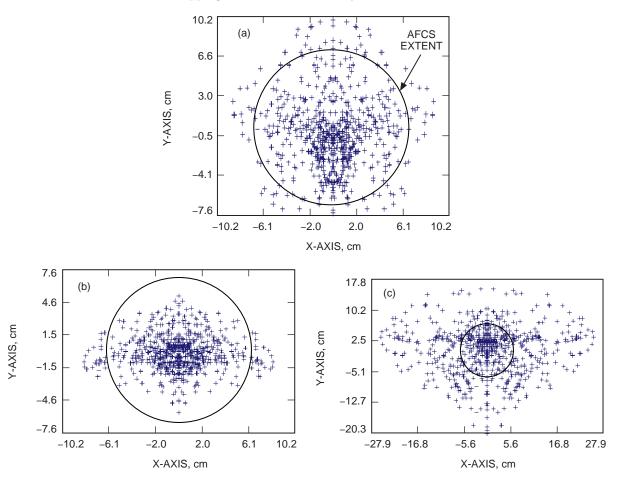

Fig. 19. Rays in the focal plane including the full extent of the AFCS for elevations of (a) 15 deg, (b) 45 deg, and (c) 85 deg.
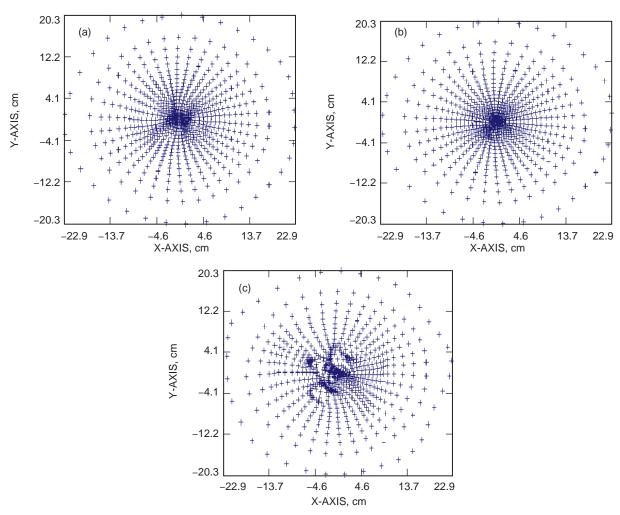
17

Fig. 20. Rays hitting the DFP (all rays hit the DFP) for elevations of (a) 15 deg, (b) 45 deg, and (c) 85 deg. The DFP diameter is 68.6 cm, and the area shown is 45.7 cm.

(4) The DFP readjusts the beam to put the peak on the mechanical boresite.

When the dish is distorted because of gravity, the main beam generally is distorted and scanned from the mechanical boresite direction (see Fig. 21(a) for 75-deg elevation). The DFP both corrects the beam shape and puts the beam peak on the mechanical boresite [see Fig. 21(b)]. The combined gain plot for the AFCS for this case (Fig. 22) shows that the array does not put the beam peak on the mechanical boresite. The combined gain plot of Fig. 22(b) is not a pattern plot but shows the maximum possible gain of the array in each of the given directions. This plot is useful for determining the optimum gain of the AFCS. However, if the AFCS is used in conjunction with the DFP, since the DFP puts the center-horn peak on the mechanical boresite, the combined gain of the AFCS is also on the mechanical boresite (see Fig. 23).

(5) When using the DFP, the monopulse null points in the direction of the main beam peak.

As mentioned earlier, when the dish is distorted, the main beam generally is misshapen and scanned from the mechanical boresite and, in general, the monopulse tracking system would not necessarily point in the direction of the main-beam peak. However, as can be seen in Fig. 24, the difference pattern as well as the sum pattern points in the direction of the mechanical boresite and, consequently, the sum and difference patterns are co-aligned.
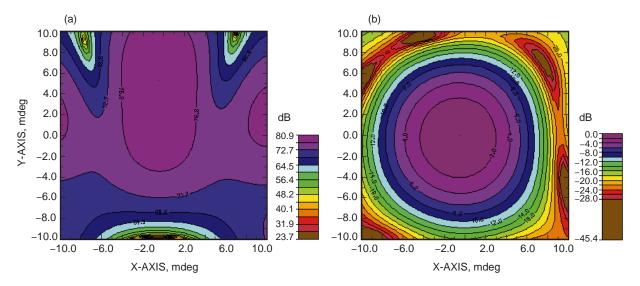
Fig. 21. The DFP readjusts the beam to put the peak on the mechanical boresite (75-deg elevation): (a) no DFP compensation (interpolated data, autolevel on, y-component) and (b) DFP compensation (interpolated data, defined levels, y-component).
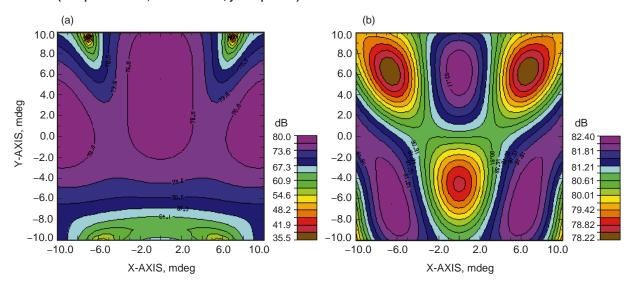

Fig. 22. The AFCS combined gain at 75-deg elevation: (a) center horn (interpolated data, autolevel on, y-component) and (b) combined gain (interpolated data, autolevel on, y-component).

(6) The current AFCS cannot provide vernier beam steering.

In Fig. 25, the maximum gain possible from the AFCS at each point on the −20 to 20 mdeg grid is plotted. An undistorted antenna is assumed for these calculations. As expected, maximum gain is produced on axis. In addition, nearly identical gain is produced at six other locations. These locations correspond to excitations in one of the six outer horns with essentially zero amplitude in each of the other horns. For regions between these peaks, the maximum gain falls to more that 10-dB below this peak and drops to nearly zero outside these six peaks.

Figure 25 shows that the AFCS provides essentially no electronic scan capability. It is capable of providing seven distinct, non-overlapping beams in the far field. This is expected due to the large gain of the individual AFCS elements. Arrays with significant scan capability typically
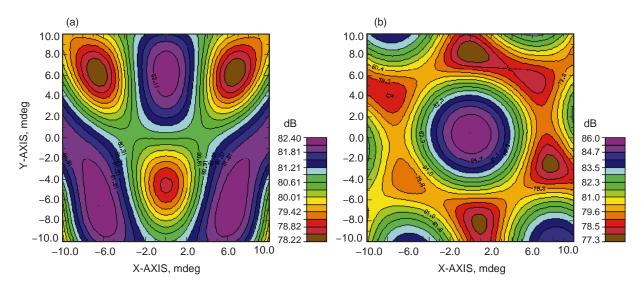
19

Fig. 23. The combination of the AFCS plus the DFP puts the beam peak on the mechanical boresite and provides significantly more gain than either system alone (75-deg elevation): (a) AFCS alone (interpolated data, autolevel on, y-component) and (b) AFCS plus DFP (interpolated data, autolevel on, y-component).
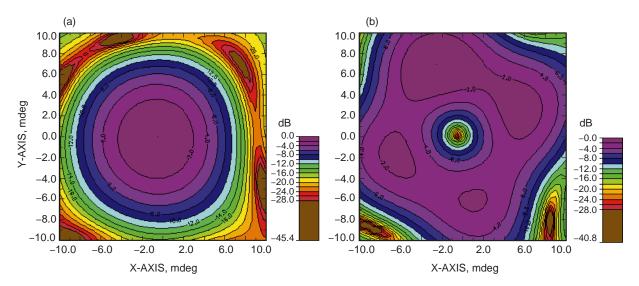

Fig. 24. The monopulse null points in the direction of the main beam peak (the monopulse feed at 75 deg with the DFP flexed): (a) sum (interpolated data, defined levels, y-component) and (b) difference (interpolated data, defined levels, y-component).

are constructed with element sizes on the order of a wavelength or less and a high ratio of effective aperture to physical aperture. The AFCS horns are over four wavelengths in diameter and have highly tapered aperture distributions.

Figure 26 shows the gain of the center feed and the maximum gain available from the AFCS for scanning in two planes. The x-scan plane corresponds to the favorable situation depicted in the figure, while the y-scan corresponds to the unfavorable situation. For scans of less than 5 mdeg around the antenna boresite, the AFCS provides nearly zero additional gain relative to the center feed alone. In the favorable situation, it recovers almost the total available gain, minus some small scan loss, for a distinct scan angle of approximately 15 mdeg.
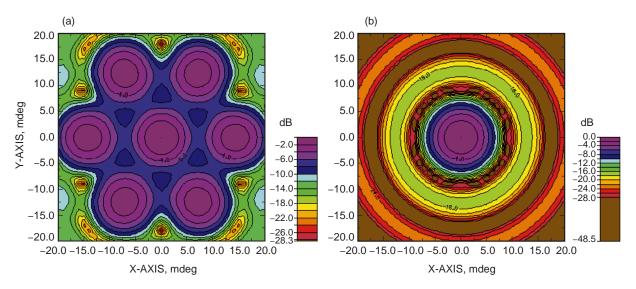
Fig. 25. AFCS electronic scanning contour plots: (a) far-field combined gain (interpolated data, defined levels, y-component) and (b) far-field center horn (interpolated data, defined levels, y-component).
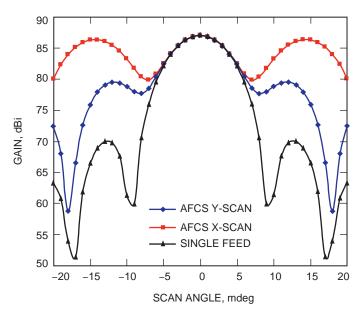

Fig. 26. AFCS electronic scanning: linear cuts.

(7) Neither the AFCS nor the DFP corrects for small errors in subreflector offset.

The AFCS has the capability to correct for some of this real-time gain loss by electronically recombining the signals in an optimum way. As an example, we consider the simple case of defocus, electronically compensating for the inability to move the subreflector in response to real-time effects. For the following calculation, we assume a perfect antenna except for a subreflector defocus.

The situation in the focal plane is depicted in Fig. 27. A simple defocus will increase the spot size in the focal plane of the antenna. For a small defocus, we expect very little of the energy will spill past the center feed. Because of the defocus, the shape of the distribution

will not match the feed distribution exactly, and some of this power will be reflected off the center feed. Thus, we do not expect the AFCS to provide excellent compensation for small defocus. For a large defocus, significant energy may fall into the outer ring of feeds, and a more significant improvement in gain may be expected from the AFCS.

A simulation of the ability of the AFCS to compensate for defocus was carried out using physical optics. The results are presented in Fig. 27. For a subreflector defocus of 0.89 cm, the predicted gain loss is 3.5 dB. The AFCS is capable of recovering 1.0 dB of this loss. Note, however, that for very small motions (0.15 to 0.4 cm) there is almost no improvement from the AFCS.

Since there is no adjustment of the DFP for real-time effects like subreflector motion, the DFP offers no correction for such effects.

VIII. Conclusions

Either system provides partial distortion correction, and the combined AFCS–DFP system both analytically and experimentally does an excellent job of distortion compensation. We also have shown that, with an accurate knowledge of the surface, a perfectly shaped DFP alone can provide significant distortion compensation.
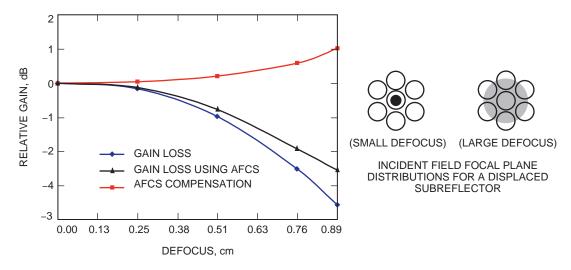

Fig. 27. AFCS defocus compensation.

References

[1] P. Richter, M. Franco, and D. Rochblatt, "Data Analysis and Results of the Ka-Band Array Feed Compensation System–Deformable Flat Plate Experiment at DSS 14," *The Telecommunications and Mission Operations Progress Report 42-139, July–September 1999*, Jet Propulsion Laboratory, Pasadena California, pp. 1–29, November 15, 1999.
http://tmo.jpl.nasa.gov/tmo/progress_report/42-139/139H.pdf

[2] V. Vilnrotter and D. Fort, "Demonstration and Evaluation of the Ka-Band Array Feed Compensation System on the 70-Meter Antenna at DSS 14," *The Telecommunications and Mission Operations Progress Report 42-139, July to September 1999*, Jet Propulsion Laboratory, Pasadena California, pp. 1–17, November 15, 1999.
http://tmo.jpl.nasa.gov/tmo/progress_report/42-139/139J.pdf

[3] D. J. Rochblatt, D. J. Hoppe, W. A. Imbriale, M. Franco, P. H. Richter, P. M. Withington, and H. J. Jackson, "A Methodology For The Open Loop Calibration Of A Deformable Flat Plate On a 70-Meter Antenna," AP2000 Millennium Conference on Antennas and Propagation, Davos, Switzerland, April 2000.

[4] *Modeling and Analysis for Controlled Optical Systems User Manual*, Version 2.4.1, Jet Propulsion Laboratory, Pasadena, California, April 1, 1997.

[5] R. Bruno, W. Imbriale, M. Moore, and S. Stewart, "Implementation of a Gravity Compensation Mirror on a Large Aperture Antenna," AIAA Multidisciplinary Analysis and Optimization Conference, Bellevue, Washington, September 1996.

[6] W. A. Imbriale and R. E. Hodges, "The Linear Phase Triangular Facet Approximation in Physical Optics Analysis of Reflector Antennas," *Applied Computational Electromagnetic Society*, vol. 6, no. 2, pp. 74–85, Winter 1991.